Turbulent Structure of a Shear-Driven Stratus-Topped Atmospheric Boundary Layer: A Comparison of Model Results with Observations

P. G. DUYNKERKE

Free University, Amsterdam, The Netherlands

A. G. M. DRIEDONKS

Royal Netherlands Meteorological Institute, De Bilt, The Netherlands

(Manuscript received 19 October 1987, in final form 2 March 1988)

ABSTRACT

An observational study of the cloud-topped atmospheric boundary layer (ABL) during a strong gale reveals that the turbulent boundary layer was dominated by shear instead of convection. A one-dimensional ensemble-averaged model is used to study this type of cloud-topped ABL. Turbulence closure is formulated by using an equation for both the turbulent kinetic energy and the viscous dissipation. The radiation model consists of an emissivity model for the longwave radiation and a two-stream model for the shortwave radiation. Both model results and observations indicate that the longwave radiative cooling at cloud top is mainly balanced by entrainment of warm air from above the inversion. A parameterization for the rainfall is included and the effect of this on the liquid water content is studied.

1. Introduction

Nicholls and Leighton (1986, hereafter referred to as NL86), discuss results from six flights in marine stratiform cloud-topped boundary layers around the United Kingdom in a variety of conditions. On five of the flights, turbulent mixing in the cloud layer was found to be maintained primarily by convection resulting from longwave radiative cooling at cloud top. As a result of the convection, cellular patterns were seen in the top of the cloud layer, which NL86 therefore classified as *stratocumulus*. However, on one of the flights (flight 564), the cellular patterns associated with convective motions within the cloud were absent. In that case the top of the cloud layer was flat, uniform and featureless, and NL86 therefore classified it as *stratus*. In this paper we will present a model simulation of this cloud-topped atmospheric boundary layer in order to examine its vertical turbulent structure.

On flight 564, shear-induced mixing dominates throughout the boundary layer. Moreover, the shear at cloud top very effectively promotes entrainment of warm air from above the inversion. Together with the subsidence the entrainment more than offsets the longwave radiative cooling at cloud top. As a result, no convection is observed and the boundary layer structure is nearly neutral. Very similar conditions were found by Brost et al. (1982a,b) in a stratocumulus deck off the California coast on 17 June 1976.

2. Model

The model used has been extensively described in Duynkerke and Driedonks (1987), with slight modifications as described in Duynkerke (1988). No tuning has been carried out for this simulation. In the one-dimensional model we have ensemble-averaged equations for the horizontal velocities (u and v), entropy (θ_q) and total water content (q_w). The vertical velocity has to be prescribed. The turbulent fluxes are modeled with the gradient approach in which the exchange coefficient is calculated from the turbulent kinetic energy (E) and the viscous dissipation (ϵ), the so called E–ϵ model. In the entropy equation we have heating or cooling due to the radiative-flux divergence. In the radiation model described in Duynkerke and Driedonks (1987), we neglected the radiative-flux divergence outside the cloud layer. Moreover we prescribed the e-folding depth for the shortwave radiative heating. Since then we have updated the radiation model with a more general model that includes the flux divergence outside the cloud layer. In addition, it explicitly resolves the profile of the shortwave radiative heating within the cloud. The radiation model used will be described below.

Corresponding author address: Dr. P. G. Duynkerke, Royal Netherlands Meteorological Institute, P.O. Box 201, 3730 AE de Bilt, The Netherlands.

a. Longwave radiation

We use the emissivity or "grey-body" approximation to calculate the upward ($F^{\uparrow}$) and downward ($F^{\downarrow}$) longwave radiative fluxes (Rodgers 1967):

$$F^{\downarrow} = \int_z^{\infty} B(T(z')) \frac{\partial \epsilon}{\partial z'}(z', z)dz', \qquad (1a)$$

$$F^{\uparrow} = \int_z^{0} B(T(z')) \frac{\partial \epsilon}{\partial z'}(z, z')dz' + B(T_B)[1 - \epsilon(z, 0)], \qquad (1b)$$

in which B is the Planck function σT^4, $\epsilon(z, z')$ is the emissivity for corrected mass of absorber $u(z, z')$ corresponding to vertical path from z to z', and T_B is the equivalent blackbody temperature, which we will take as equal to the sea-surface temperature T_s.

The emissivity in (1) is calculated as

$$(1 - \epsilon) = (1 - \epsilon_v)(1 - \epsilon_{CO_2})(1 - \epsilon_c), \qquad (2)$$

in which v stands for vapor, CO_2 for carbon dioxide and c for cloud. Rodgers (1967) gives suitable schemes for water vapor and CO_2. Welch and Zdunkovski (1976) have discussed a revised scheme for water vapor. We use (2) with

$$\epsilon_v = \epsilon_{v1}(u) + \epsilon_{v2}\left(\frac{ue}{p_*}\right), \qquad (3)$$

in which u is the corrected mass of water vapor absorber

$$u = \left|\int_z^{z'} \rho q_v (p/p_*)^{0.9} dz\right| \qquad (4)$$

and e is the partial vapor pressure

$$e = \frac{pq_v}{\epsilon - q_v(\epsilon - 1)}. \qquad (5)$$

For $\epsilon_{v1}(u)$ we have used the scheme presented by Welch and Zdunkovski (1976). The second term in (3), $\epsilon_{v2}(ue/p_*)$ represents the effect of the water vapor dimer within the window region, for which we use the parameterization of Stephens and Webster (1979). For $\epsilon_{CO_2}(u_{CO_2})$ we have used the scheme given by Rodgers (1967) in which

$$u_{CO_2} = \left|\int_z^{z'} 100C\left(\frac{\rho}{\rho_*}\right)\left(\frac{p}{p_*}\right)^{0.9} dz\right|, \qquad (6)$$

where $C = 330 \times 10^{-6}$ ppm at all levels and u is in cm atm. For $\epsilon_c(W)$ we have used the scheme given by Stephens (1978) in which

$$W = \left|\int_z^{z'} \rho q_l dz\right|. \qquad (7)$$

b. Shortwave radiation

The shortwave radiative fluxes are calculated using a model (SUNRAY) described by Fouquart and Bonnel (1980). Our major departure from Fouquart and Bonnel's parameterization is that we use the δ-Eddington approximation instead of the exponential kernel. The model involves Rayleigh scattering, absorption by atmospheric gases (water vapor, ozone and CO_2) and absorption and scattering by cloud droplets. The cloud radiative properties are defined as in Fouquart and Bonnel (1980) and are based on the optical thickness of a layer (τ). The optical thickness is calculated from: $\tau = 3W/2r_e$, where r_e is the equivalent radius of the droplet distribution (set to 10 μm) and W is the liquid water mass defined in (7). The single scattering albedo of the droplets is given by Fouquart and Bonnel (1980):

$$\omega_0 = 0.9989 - 4 \times 10^{-3} \exp(-0.15\tau_t), \qquad (8)$$

where τ_t is the optical thickness of the whole cloud layer.

3. Synoptic conditions

A weak low-pressure system was situated between the southern tip of Greenland and Iceland at 1200 UTC 13 December 1982. As the accompanying occluded front moved northeastward an unstable wave developed. This can be seen in the surface pressure map at 1200 UTC 14 December shown in Fig. 1a. From this wave a new low-pressure system developed and deepened very rapidly. At 1200 UTC 15 December this new low-pressure system was located just off the west coast of Norway and had reached a pressure of 950 mb at its core (Fig. 1b). At this time the original low-pressure system was located southwest of Iceland, and it would ultimately merge with the newly developed cyclone. The measurements described by NL86 (case 564) were taken between 1000 and 1512 UTC 15 December 1982 around 50.21°N, 6.38°W. The area of measurement is located in the warm sector of the cyclone, which was strongly influenced by the high-pressure system off the west coast of Spain.

In order to show the vertical structure of the atmosphere around the measuring area, we have plotted the radiosonde profiles from Valentia (03953; 51.56°N, 10.15°W), Camborne (03808; 50.13°N, 5.19°W) and Brest (07110; 48.27°N, 4.25°W) at 1200 UTC 15 December (Fig. 2). The temperature and dewpoint profiles at Camborne are very similar to those measured by NL86, except for the maximum in mixing ratio just above the inversion (which might be a measurement error due to the evaporation of water droplets on the radiosonde). In Camborne the surface temperature is 10.4°C, whereas NL86 gives a sea surface temperature of 10.3°C. Moreover, the radiosonde profile shows an inversion height of about 900 m, whereas NL86 gives 850 m. In Camborne the windspeed at the inversion is 50 knots. At all three stations (Fig. 2) the sky was reported to have been completely covered with stratus. The cloud base observed at Camborne was between 100 and 200 m, compared to 180 m observed by NL86.

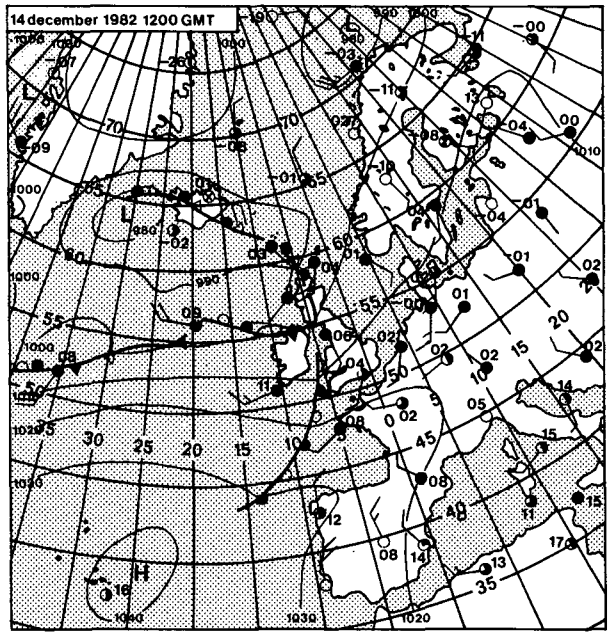

FIG. 1a. Synoptic surface map for 1200 UTC 14 December 1982.

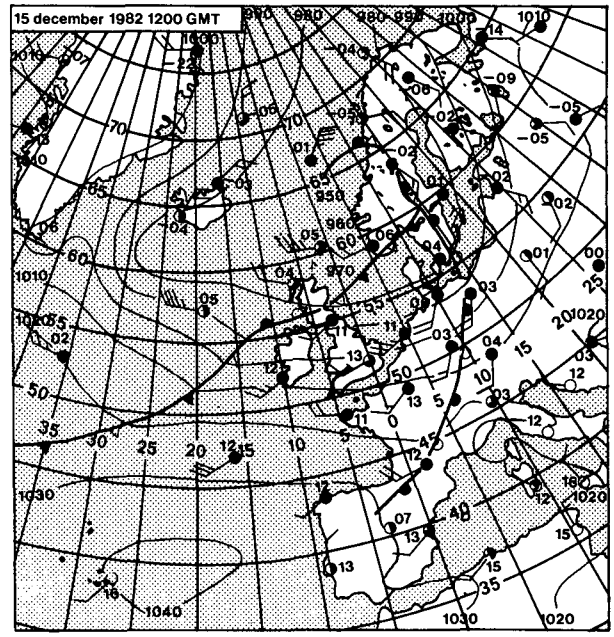

FIG. 1b. Synoptic surface map for 1200 UTC 15 December 1982.

We can therefore conclude that the Camborne radiosonde data are in good agreement with the values observed by NL86 over the sea.

The radiosonde profiles in the nearby stations at Brest and Valentia (Fig. 2), however, show quite a different vertical structure, especially above the boundary layer. We may therefore conclude that the lower atmosphere (up to ~2000 m) in the region of measurement is not horizontally homogeneous on the scale of several hundreds of kilometers.

4. Model results and comparison with observational data

The measurements of case 564 were taken around noon 15 December 1982. The observations show that at this time of year, the total shortwave absorption inside the cloud is quite small (~15 W m^{-2}). The air is slightly warmer than the sea causing a virtual heat flux ($\rho c_p \overline{w'\theta_v'}$) at the surface of about −20 W m^{-2}. Due to the stable stratification near the surface, no convection from the sea surface is generated. Although the observations show a strong longwave radiative cooling (78 W m^{-2}) at cloud top, no convection is observed in the cloud layer.

Nicholls and Leighton note that in case 564 shear production dominates throughout the depth of the boundary layer. This is a result of the strong winds in the boundary layer (~30 m s^{-1}), with little variation up to the atmospheric boundary layer (ABL) height where quite strong jumps occurred. The locally strong wind shear generated significant entrainment of warm air from above the inversion. Together with the subsidence the entrainment warming balances the longwave radiative cooling at cloud top, and the buoyancy flux is negative throughout the boundary layer (*no* convection). Cloud top processes were therefore hardly felt farther down in the ABL, and as a result, the ABL showed a near-neutral structure, in which shear production was almost locally balanced by dissipation.

The model simulation was set up to see whether this type of turbulence structure could be simulated. The run was done for a latitude of 50°N and longitude of 0°W. In the neutral boundary layer the time scale $2\pi/f$ (~15 hours) is dominant. In order to get winds that are fairly stationary in the boundary layer, we will present model results after a simulation time of 24 hours. The model run was started at local noon 15 December. We initialized the model with values close to those observed by NL86. A divergence of 1.1×10^{-5} s^{-1} was applied to limit the rise of the mean cloud top. The initial wind components u and v were set equal to their geostrophic values of 30 and −8 m s^{-1}, respectively. The inversion height was set to the observed value of 850 m. Below the inversion we initialized θ_q = 304.5 K, and above the inversion θ_q = 312.5 K and $q_w = 7.4\text{–}8 \times 10^{-2}$ g kg^{-1} (z in m) up to the model top. The sea surface temperature was set at T_s = 283.3 K, the specific humidity was set equal to its saturated value at the surface $q_w = q_{vsat}(T_s)$, and the surface pressure was 1009 mb. The roughness length was determined from Charnock's relation $z_0 = \alpha(u_*^2/g)$ with α = 0.014 (Haltiner and Williams 1980), which gives $z_0 = 8 \times 10^{-4}$ m.

The u and v wind profiles after a simulation time of 24 hours are plotted in Fig. 3 together with the observed

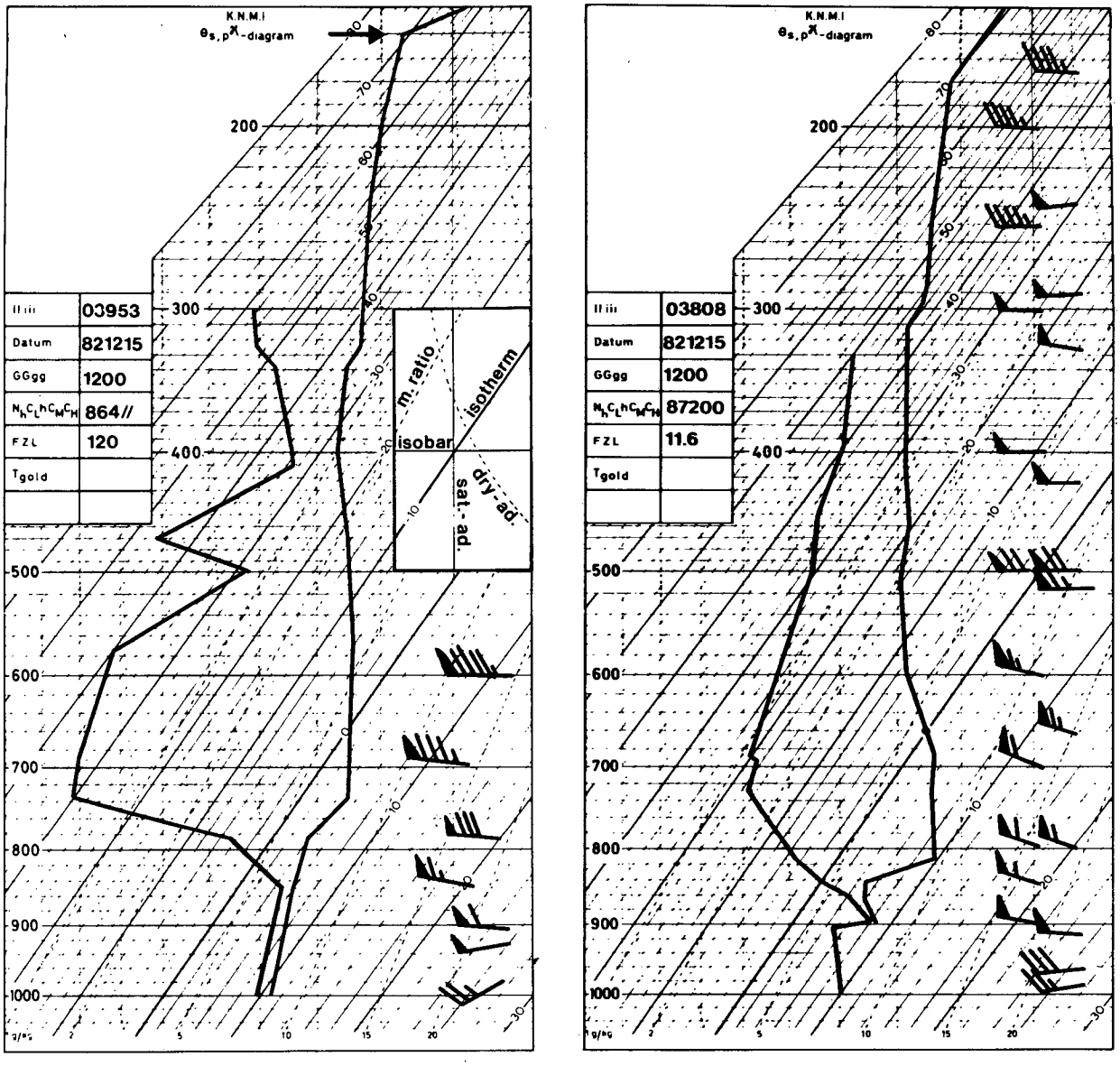

FIG. 2. Radiosonde profiles of dewpoint (left) and temperature (right) at 1200 UTC 15 December for Valentia, Camborne and Brest, respectively.

values from NL86. It can be seen that the v-component of the wind is rather well mixed throughout the ABL. At the inversion, the model gives jumps in the wind $\Delta v \approx -6$ m s^{-1} and $\Delta u \approx -2$ m s^{-1} compared to observed values of -6 m s^{-1} and -3 m s^{-1}, respectively. The observations indicate a slightly larger turning of the wind close to the surface, which might be due to the inhomogeneity mentioned in section 3.

In Figs. 4 and 5 the observed, initial and calculated profiles of T, q_w and q_l are shown together with the observations. The initial temperature difference between the sea surface and the air just above is about 1°C. The model results give a Monin-Okukhov length $L = 1550$ m, and thus the stability has only a small effect on the turbulence due to the extremely high wind speed. At the inversion there is a temperature jump of about 6°C. Due to the applied subsidence, a net warming takes place above the inversion. The predicted liquid water content (Fig. 5) is about twice as large as the observed liquid water content. Later it will be shown that this discrepancy can be explained by taking gravitational droplet settling into account (section 4). In Table 1 we have compared the calculated longwave and shortwave radiative fluxes above and below the stratus layer with both the observed values and the values calculated with the model used by NL86. The model gives a net cooling of 67 W m^{-2} over the whole cloud layer due to longwave radiation compared to an

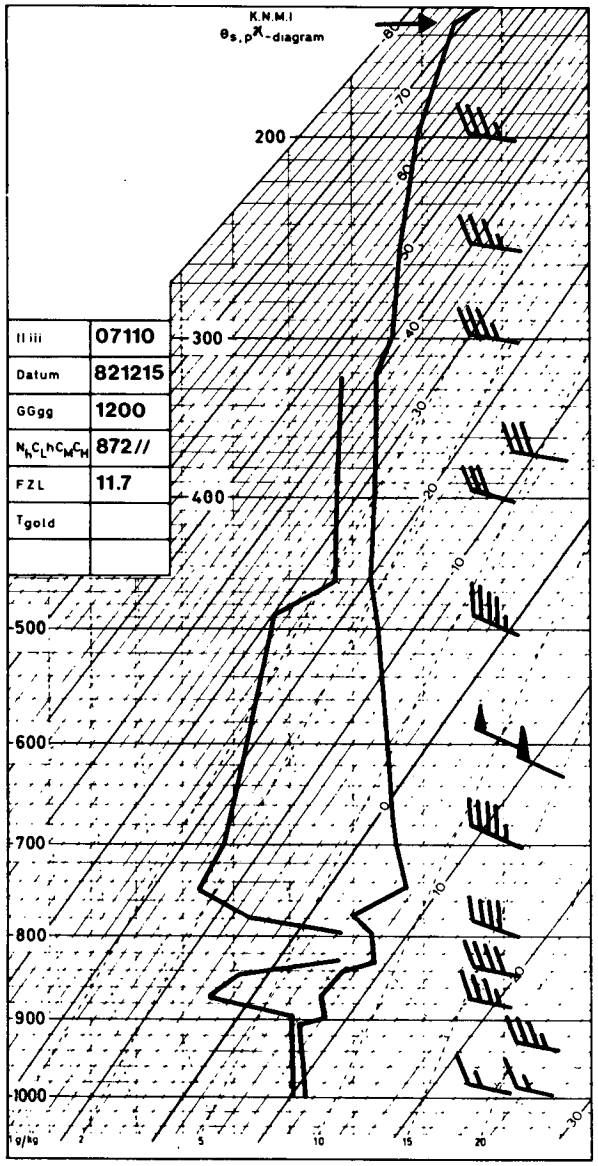

FIG. 2. (*Continued*)

observed value of 70 W m^{-2}. The calculated absorption of shortwave radiation equals 15 W m^{-2} (Table 1). As discussed above, in this case the longwave radiative cooling at the cloud top is not promoting convection because it is locally balanced by the entrainment and subsidence of warm air. We will demonstrate this by showing some vertical profiles of turbulence quantities and discuss their effect on the structure of the ABL.

Profiles of the calculated stresses are compared with the observed values in NL86 in Fig. 6. The zonal component of the stress decreases linearly with height up to the inversion. By considering the zonal component of the momentum equation

$$f(v - v_g) = \frac{\partial \overline{u'w'}}{\partial z}, \tag{9}$$

it follows that $(v - v_g)$ should be constant within the mixed layer, as can be seen in Fig. 3. Integrating (9) from $z = z_0$ to above the inversion and assuming that $v - v_g$ is constant throughout the mixed layer, we get

$$\Delta v = -\frac{u_*^2}{fh}.$$

Both the $\overline{uw}$ and $\overline{vw}$ profiles are very similar to those observed by Nicholls (1985) (during the JASIN experiment), which are representative for the near-neutral ABL. In those cases the boundary layer was nearly neutral, and its growth was inhibited by a stable lapse rate aloft. This has been extensively discussed in Duynkerke (1988). In Fig. 6 we have also plotted the corresponding values for zf/u_*, which show that the depth of the boundary layer is about $0.11u_*/f$, whereas Nicholls (1985) found a depth of approximately $0.2u_*/f$. This lower boundary layer depth may be a result of the stronger inversion in this case.

Observations similar to those of Nicholls (1985) have been made by Grant (1986), who found a boundary layer depth of about $0.1u_*/f$. The observed boundary layer height and turbulent fluxes in case 564 are thus in good agreement with values observed in other near-neutral ABLs.

The terms in the turbulent kinetic energy equation are shown in Fig. 7. Throughout the entire boundary layer, the shear production (S) is almost locally balanced by viscous dissipation (D), whereas the buoyancy term (B) and transport of TKE (T) are small. As a result, a neutral ABL is formed. Near the inversion the shear production has a local maximum due to the velocity jumps shown in Fig. 3. This causes an enhanced entrainment of warm air from above the inversion. Figure 8 shows the calculated TKE-profile and the measured $\bar{w}^2$-profile (we have no data for $\bar{u}^2$ and $\bar{v}^2$), both made dimensionless with u_*^2 and plotted as a function of z/h in which $h = 0.11u_*/f$. If convection due to longwave radiative cooling at cloud top were present, the $\bar{w}^2$-profile would show a maximum inside the cloud layer (NL86). However, both the calculated TKE-profile and the measured $\bar{w}^2$-profile decrease continuously with height and thus reveal that the structure of the ABL is neutral, as found by Nicholls (1985) and Grant (1986).

The observed virtual temperature flux data are compared with the calculated profile in Fig. 9. Both observations and calculations show that the boundary layer is slightly (Fig. 7) stable up to the inversion. The calculated profile shows much more vertical structure than the observations: in the cloud, $\overline{w\theta_v}$ is small with minima near the inversion and below cloud. Due to the horizontal variations in the boundary layer depth and the horizontal averaging used to obtain the observational fluxes, it is almost impossible to resolve the minimum in the virtual temperature flux near cloud top. From this minimum, according to both the model and

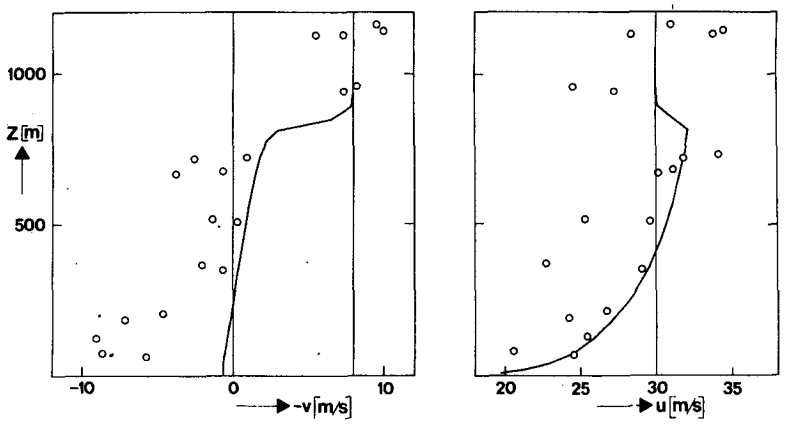

FIG. 3. Comparison of observed (circles) and modeled (thick lines) wind speed. Thin lines are initial conditions.

the observational results, it seems that the cloud top in the model is slightly higher than in the observations.

In the model the boundary layer depth is almost constant in time; therefore the entrainment velocity (w_e) equals the subsidence velocity at cloud top, which has a value of 0.9 cm s^{-1}. From the observations, NL86 estimated the entrainment velocity to be about 1.2 cm s^{-1}, with an uncertainty of 30% to 50%. The entrainment velocity calculated with the model is thus somewhat smaller than the value estimated from observations, but within the uncertainty interval.

The calculated virtual temperature flux (Fig. 9) at the surface ($\approx -2.7 \times 10^{-2}$ K m s^{-1}) is smaller than the observed value ($\approx -1.8 \times 10^{-2}$ K m s^{-1}). This might be a result of the fact that the $w\theta_v$-flux at the surface is very sensitive to the value of the prescribed sea surface temperature. From the radiation thermometer NL86 estimated the sea surface temperature to be 283.3 ± 0.5 K. We used T_s = 283.3 K. An increase in the sea surface temperature of about 0.3 K is sufficient to obtain the observed virtual temperature flux in the model. The influence of stability on the turbulence, however, remains small, as discussed above. In Fig. 10 both calculated and observed moisture fluxes are shown. The observations show considerable scatter from which no clear conclusions can be drawn. The calculated profile indicates that the input of moisture from the sea surface is about as large as the entrainment of dry air from above the inversion. As a result, the turbulent flux is constant throughout the boundary layer and thus, the value of q_w in the ABL does not change due to turbulence.

The net longwave radiative flux, net shortwave radiative flux, and wet equivalent potential temperature flux ($\overline{w'\theta'_q}$) are displayed in Fig. 11. The longwave radiative cooling at the cloud top is mainly balanced by entrainment ($\overline{w'\theta'_q}$) and subsidence (not shown). Therefore, the cooling at cloud top does not generate a positive buoyancy flux (*no* convection!) (Fig. 9).

The effect of rainfall rate. From the preceding comparison between the calculations and observations, we conclude that the model simulates the observed structure of case 564 quite well. One of the clearest differ-

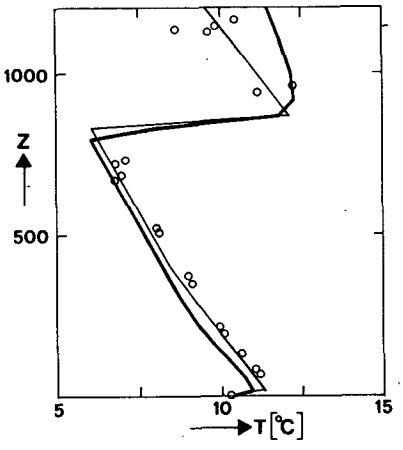

FIG. 4. As in Fig. 3 but for temperature.

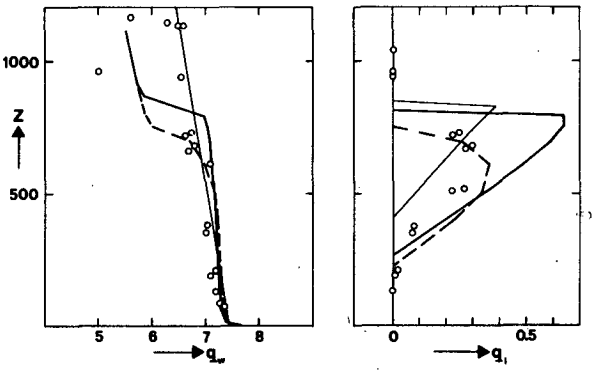

FIG. 5. As in Fig. 3 but for the specific water content (q_w) and the specific liquid water content (q_l). The dashed lines are model results in which gravitational droplet settling has been taken into account.

TABLE 1. Cloud longwave and shortwave properties: observations and model results of Nicholls and Leighton (1986); results with present model.

	Observed (NL86)	Model (NL86)	Present model
$F_L^{\uparrow+}$	345	354	349
$F_L^{\downarrow+}$	267	246	277
$F_L^{\uparrow-}$	366	362	363
$F_L^{\downarrow-}$	358	357	358
$F_L^{\uparrow+} - F_L^{\uparrow-}$	−21	−8	−14
$F^{\downarrow+} - F^{\downarrow-}$	−91	−111	−81
$F_L^{+} - F_L^{-}$	70	103	67
$F_S^{-} - F_S^{+}$	−19	17	15

ences was that the model predicted a liquid water content twice as high as the observed value. Here we will show that this might be due to gravitational settling of droplets, which was not included in the model until now. In case 564 the air mass is of maritime origin, so that the droplet concentration is very small ($N \sim 35$ cm^{-3}) and the mean volume radius of the droplets is quite large ($r_v \sim 20$ μm). The cloud-top rainfall rate observed in NL86 was large (1.7×10^{-5} m s^{-1}) and of the same order as the observed moisture flux (Fig. 10). If we include the effect of gravitational settling of droplets, the equation for q_w becomes

$$\frac{\partial q_w}{\partial t} = -\frac{\partial \overline{w'q_w'}}{\partial z} - \frac{\partial \widetilde{w_T q_l}}{\partial z} - w\frac{\partial q_w}{\partial z}, \qquad (10)$$

where $\widetilde{w_T q_l}$ is the gravitational settling (or rainfall rate) following Brost et al. (1982b):

$$\widetilde{w_T q_l} = -\frac{\rho_l}{\rho_0}\int_0^\infty w_T(r)\frac{4}{3}\pi r^3 n(r)dr. \qquad (11)$$

The fall speed of a droplet of radius r is represented by w_T. Over a wide range of radii ($r \leq 40$ μm), w_T can be parameterized as: $w_T = w_0 r^2$, with $w_0 = 1.27 \times 10^8$ m^{-1} s^{-1} (Stokes flow). The number of drops per unit volume in the radius interval r to $r + dr$ is $n(r)$. If we employ the size distribution (Hansen and Travis 1974),

$$n(r) = \frac{N_0}{(ab)^{(1-2b)/b}\Gamma[(1-2b)/b]} r^{(1-3b)/b} \times \exp(-r/ab), \qquad (12)$$

in which N_0 in m^{-3} is the number of particles per unit volume, a the effective radius (r_e), b the dimensionless variance, and Γ is the gamma function. If we use Stokes flow and (12) in (11) we get

$$\widetilde{w_T q_l} = -\left(\frac{\rho_l}{\rho_0}\frac{4}{3}\pi(1-b)(1-2b)\right)^{-2/3} \times w_0(1+2b)(1+b)\frac{{q_l}^{5/3}}{{N_0}^{2/3}}. \qquad (13)$$

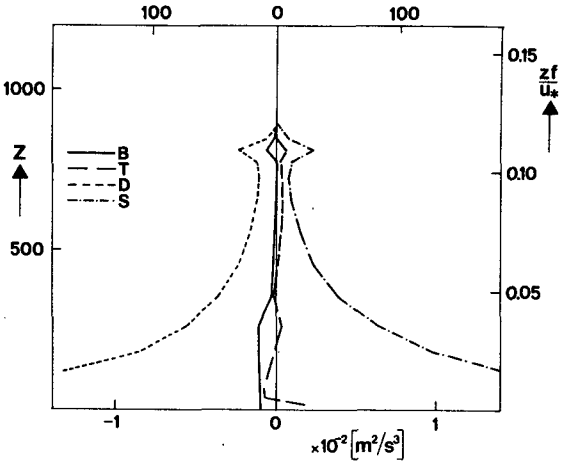

FIG. 7. The calculated turbulent kinetic energy budget: B buoyancy production; T turbulent transport; D viscous dissipation; S shear production.

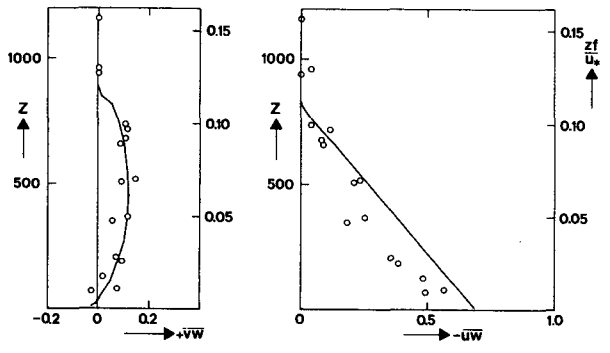

FIG. 6. Comparison of observed (circles) and calculated (curves) momentum fluxes.

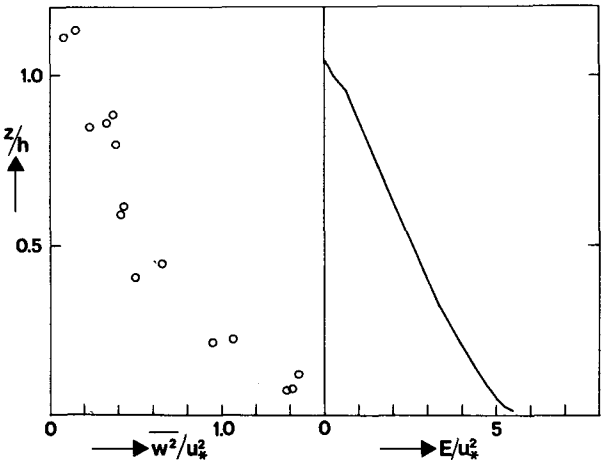

FIG. 8. Vertical velocity variance measurements (circles) and calculated turbulent kinetic energy as a function of height.

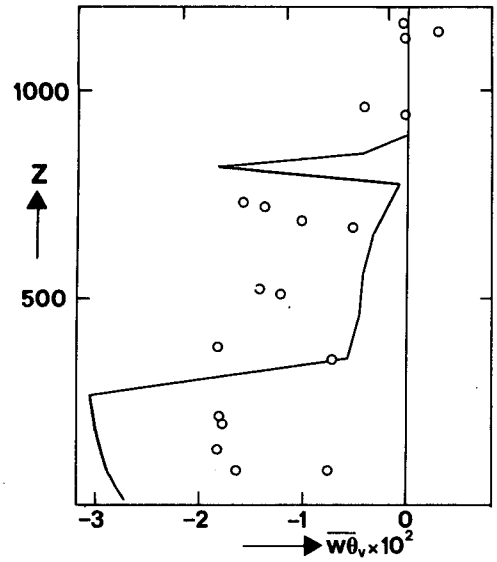

FIG. 9. As in Fig. 6 but for the virtual temperature flux.

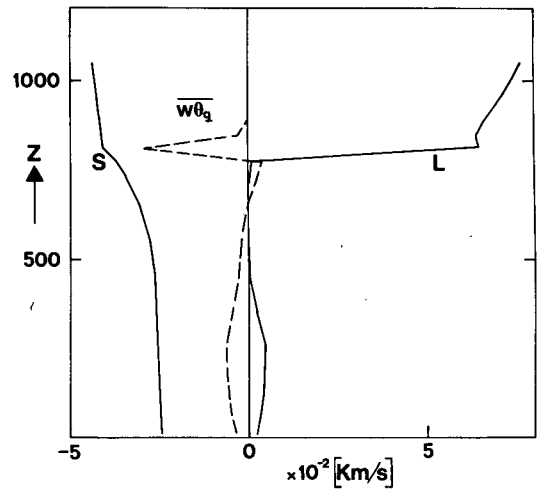

FIG. 11. The profiles of the net longwave radiative flux L, net shortwave radiative flux S, and $w'\theta_q'$ flux.

With $b \sim 0.1$ equation (13) gives

$$\widetilde{w_T q_l} \approx -1 \times 10^6 \frac{q_l^{5/3}}{N_0^{2/3}} \text{ m s}^{-1}.$$

This seems a reasonable parameterization for the rainfall rate for smaller droplets ($r \leqslant 40$ μm).

For larger droplets (which also determine the rainfall rate below cloud) we need another expression, which will be much more complicated because it depends on the details in the droplet distribution for large r. Moreover, the Stokes flow will no longer hold. Because of the complexity we have not accounted for this effect. Therefore we will not get any drizzle below cloud.

We have made the same model run as before but have now included the parameterization for the gravitational droplet settling (13) in the equation for q_w (10). Observational data (Nicholls 1984; NL86) indicate that the droplet concentration N_0 is approximately independent of height. Therefore, we have taken N_0 in (13) to be constant and equal to the observed value $N_0 = 35 \times 10^{-6}$ m^{-3} (NL86). In Fig. 12 we have compared the calculated turbulent moisture flux $\overline{w'q_w'}$ and the rainfall rate $\widetilde{w_T q_l}$ with the observed fluxes. With N_0 constant, we get from (13) that the rainfall rate (Fig. 12) is thus very similar to the liquid water profile: the value of $-\widetilde{w_T q_l}$ increases from cloud base upwards and has a maximum just below cloud top. From (10) it follows that above the maximum in the

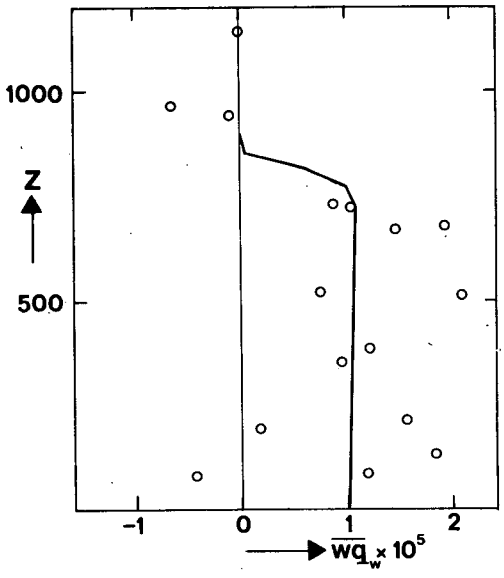

FIG. 10. As in Fig. 6 but for the total water flux.

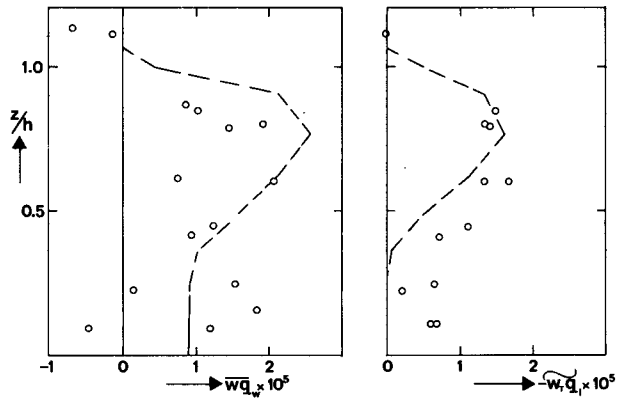

FIG. 12. Comparison of observed (circles) and calculated (dashed lines) fluxes: the flux of total water substance $\overline{w'q_w'}$; gravitational settling of droplets $\widetilde{w_T q_l}$.

rainfall rate q_w will decrease due to droplet settling, whereas below the maximum in $-\widetilde{w_T q_l}$, q_w will increase. Because q_w is almost well-mixed throughout the boundary layer, $\overline{wq}_w + \widetilde{w_T q_l}$ varies approximately linearly (here nearly constant) with height. This means that the turbulent transport $\overline{wq}_w$ will partially compensate the changes due to droplet settling. In Fig. 5 we have drawn the calculated q_w and q_l profiles, which show that, due to the gravitational droplet settling, the liquid water content has been reduced quite drastically. The calculated maximum liquid water content ($\sim$0.35 g kg^{-1}) is now just slightly larger than the observed value ($\sim$0.3 g kg^{-1}).

The liquid water content will thus be significantly reduced due to gravitational droplet settling. However, the gravitational droplet settling has little effect on the other results discussed here. Because there will be enough liquid water to ensure that the cloud radiates as a blackbody, the longwave radiative cooling at cloud top will remain almost unchanged. Moreover, the dynamics of this stratus layer are so dominated by shear that the results discussed in this paper (except, of course, for the liquid water content), will remain almost unchanged if gravitational droplet settling is included.

5. Conclusions

Observations on flight 564 (NL86) made in a strong gale show that the boundary layer was dominated by shear-driven mixing instead of convective mixing, despite the fact that the longwave radiative cooling at cloud top was quite large ($\sim$78 W m^{-2}). Both model results and observations indicate that the radiative cooling near cloud top is mainly balanced by entrainment of warm air from above the inversion. The entrainment is enhanced because of velocity jumps at the inversion. In addition, the model results show that part of the longwave radiative cooling is balanced by subsidence, which warms the air in and above the inversion. In case 564 the net result of longwave radiative cooling, entrainment, and subsidence warming is that the buoyancy flux is negative throughout the boundary layer. The buoyancy term, however, is small compared to the shear production term, and as a result a near-neutral ABL is formed. It is found that the observed turbulent structure compares well with other observations of the near-neutral ABL (Grant 1986; Nicholls 1985).

The largest discrepancy between the model results and observations is that the model tends to overpredict the liquid water content. It is shown that the prediction of the liquid water content can be improved by including gravitational droplet settling, which was important in case 564 because the air was of maritime origin. In this kind of air, the droplet concentration is small and the droplets are relatively large, resulting in a significant flux of water due to gravitational settling.

Acknowledgments. We would like to thank H. R. A. Wessels for discussions on the microphysical part of the work and H. L. Pan for reading the manuscript. A version of the original shortwave radiation program was kindly supplied by L. Smith and J. J. Morcrette when one of us (P.G.D.) was visiting Colorado State University. We are also grateful to S. Nicholls for supplying us with the experimental data on flight 564.

REFERENCES

Brost, R. A., D. H. Lenschow and J. C. Wyngaard, 1982a: Marine stratocumulus layer. Part I: Mean conditions. *J. Atmos. Sci.*, **39**, 800–817.

——, —— and ——, 1982b: Marine stratocumulus layers. Part II: Turbulence budgets. *J. Atmos. Sci.*, **39**, 818–836.

Duynkerke, P. G., 1988: Application of the E–ϵ turbulence closure model to the neutral and stable atmospheric boundary layer. *J. Atmos. Sci.*, **45**, 865–880.

——, and A. G. M. Driedonks, 1987: A model for the turbulent structure of the stratocumulus-topped atmospheric boundary layer. *J. Atmos. Sci.*, **44**, 43–64.

Fouquart, Y., and B. Bonnel, 1980: Computations of solar heating of the earth's atmosphere: A new parameterization. *Beitr. Phys. Atmos.*, **53**, 35–62.

Grant, A. L. M., 1986: Observations of boundary layer structure made during the 1981 KONTUR experiment. *Quart. J. Roy. Meteor. Soc.*, **112**, 825–841.

Haltiner, G. J., and R. T. Williams, 1980: *Numerical Prediction and Dynamic Meteorology.* Wiley & Sons, 477 pp.

Hansen, J. E., and L. D. Travis, 1974: Light scattering in planetary atmospheres. *Space Sci. Rev.*, **16**, 527.

Nicholls, S., 1984: The dynamics of stratocumulus: Aircraft observations and comparison with a mixed layer-model. *Quart. J. Roy. Meteor. Soc.*, **110**, 783–820.

——, 1985: Aircraft observations of the Ekman layer during the Joint Air–Sea Interaction Experiment. *Quart. J. Roy. Meteor. Soc.*, **111**, 391–426.

——, and J. Leighton, 1986: An observational study of the structure of stratiform cloud sheets: Part I: Structure. *Quart. J. Roy. Meteor. Soc.*, **112**, 431–460.

Rodgers, C. D., 1967: The use of emissivity in atmospheric radiation calculations. *Quart. J. Roy. Meteor. Soc.*, **93**, 43–54.

Stephens, G. L., 1978: Radiation profiles in extended water clouds. Part II: Parameterizations schemes. *J. Atmos. Sci.*, **35**, 2123–2132.

——, and P. J. Webster, 1979: Sensitivity of radiative forcing to variable cloud and moisture. *J. Atmos. Sci.*, **36**, 1542–1556.

Welch, R., and W. Zdunkowski, 1976: A radiation model of the polluted atmospheric boundary layer. *J. Atmos. Sci.*, **33**, 2170–2184.